Åsmund Fossum

Bachelor's thesis

Assessment of Noise Production from Airfoils for Wind Turbines

May 2022

NTNU
Norwegian University of Science and Technology
Faculty of Engineering
Department of Energy and Process Engineering

NTNU
Norwegian University of
Science and Technology

Bachelor's thesis

2022

NTNU
Norwegian University of
Science and Technology

Åsmund Fossum

Assessment of Noise Production from Airfoils for Wind Turbines

Bachelor's thesis
May 2022

NTNU
Norwegian University of Science and Technology
Faculty of Engineering
Department of Energy and Process Engineering

NTNU
Norwegian University of
Science and Technology

Preface

The work described in this Bachelor thesis is conducted during the spring 2022 at NTNU in cooperation with Sintef. This thesis is written during the subject "FENT2900 Bachelor thesis, renewable energy", and finishes a three-year Bachelor study in renewable energy engineering at NTNU, Norwegian University of Science and Technology. The project has given a deep and interesting insight into both software for airfoil noise modelling, but also into general engineering working methods. I would like to thank Balram Panjwani from Sintef for providing relevant literature, such as [1], and knowledge about the software used, as well as giving general help and advise in the subject of noise modelling. I would also like to thank my supervisor Tania Bracchi from NTNU for help with theory and logistics through the whole project process. Lastly, I want to thank Julien Christophe from IVKDF (The von Karman Institute for Fluid Dynamics) for general guidance and providing noise results from IVKDF's simulation models.

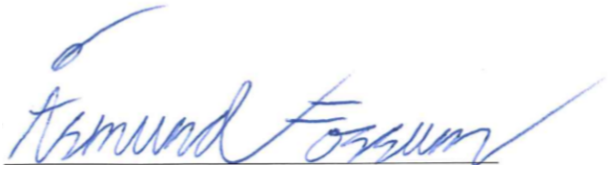

Åsmund Fossum

Abstract

Wind energy is a promising way of renewable energy production, and new wind parks are being built at faster rate than ever before. However, wind parks are met with local protests many places, and one of the protesters' arguments is noise pollution. Therefore, this study aimed to simulate noise production from airfoils, which can be expanded into simulating aerodynamic noise from wind turbines. The methodology was similar to one performed by Sintef and IVKDF, which calculates the wall-pressure spectra and sound pressure levels of the three airfoils NACA0012, NACA64418 and DU96. However, the present study replaced some steps with simple and open-source methods, aiming to evaluate whether they produced sufficiently accurate results. In this study, pressure distributions were calculated by OpenFOAM's SimpleFoam solver as an alternative method, and these pressure distributions were used as inputs for calculating noise production. Intermediate results were validated, and showed acceptable agreement with references, except close to the trailing edges of the airfoils. Since this was where the noise was calculated, it led to some inaccuracies in the noise results as well. However, simple improvements in the mesh can most likely improve the results significantly, making the methodology applicable for larger studies of airfoil noise and wind turbine noise.

Sammendrag

Vindenergi er en lovende måte å produsere fornybar energi på, og det blir bygget flere nye vindparker nå enn noen gang tidligere. Likevel blir vindparker møtt med lokal motstand mange steder, og et av motstandernes argumenter er støyforurensning. Derfor var målet med denne studien å simulere støyproduksjon fra vingeprofiler, som kan utvides til å simulere aerodynamisk støy fra vindturbiner. Metoden hadde likhetstrekk med et arbeid utført av Sintef og IVKDF, som beregner veggtrykkspektra og lydtrykknivå for de tre vingeprofilene NACA0012, NACA64418 og DU96. Likevel har denne studien erstattet noen steg med enklere steg som også har åpen kildekode, for å vurdere om de produserer tilstrekkelig nøyaktige resultater. I denne studien ble trykkfordelinger beregnet ved hjelp av OpenFOAM sin SimpleFoam-kalkulator, som en alternativ metode, og disse trykkfordelingene ble brukt videre til å beregne støy. Mellomresultater ble validert, og viste akseptabelt samsvar med referanser, bortsett fra nærmere vingeprofilenes bakkanter. Siden dette også er hvor støyen ble beregnet, ga det noen unøyaktigheter i støyresultatene også. Likevel er enkle forbedringer i data-maskenettet sannsynligvis tilstrekkelig til å gi en signifikant forbedring av resultatene, og dette gjør metoden aktuell for større studier av støy fra vingeprofiler og vindturbiner.

Contents

1 Introduction

During the last few decades, the development of wind energy has increased drastically. According to the Global Wind Report 2021, the worldwide wind energy capacity had then reached 743 GW, saving CO_2 emissions equivalent to the total annual emissions of South Africa [2]. At the same time, the report claims that the wind energy installing rate has to become three times faster than the 53 % annual increase from 2020 in order to reach the goal of net zero emissions by 2050 [2].

Not only the number of wind turbines is increasing, their sizes are also increasing. The largest wind turbines today have a diameter of more than 100 m. This leads to an increased aerodynamic noise production, which is one of the problems that wind energy protesters both in Norway and elsewhere complain about [3]. In some wind parks, it has even been necessary to lower the electricity production rate because of noise pollution. Some studies also suggest that noise from wind turbines may have a significant negative impact on health-related quality of life [4]. This makes it interesting to study how noise from wind turbines is produced.

However, wind turbine noise is a complicated field of study, with different proposed methodologies. Some articles describe experiments performed with specific airfoils and operating conditions, such as [5]. Several works have also aimed to simulate noise from wind turbines, and validated their results against available experimental data. The most frequently used method is by applying RANS equations and Amiet's model. A such work is conducted by Sintef and IVKDF [1], Tian [6], Küçükosman [7] and many others. One alternative also conducted by [1] was to use the RPM method to generate turbulent velocity fluctuations. Another alternative is to apply Large Eddy Simulations (LES) and the Smagorinsky SGS model together with Curle's analogy [8]. These are only a few examples, there are several other proposed models with variable degree of accuracy.

The goal of this study was to use OpenFOAM's SimpleFoam solver to calculate the pressure distribution that was converted into noise production from three different airfoils, and validate this method and against existing references. A similar work has been conducted by Sintef and IVKDF [1], which was used as the main reference. This study performed merely the same calculations, but with the open-source OpenFOAM software package and its SimpleFoam solver instead of STAR-CCM+, as well as a simple way of creating airfoil meshes. The purpose was to study if this more simple and open-source software was able to produce sufficiently accurate noise results. Conclusions about the methodology's validity and possible improvements were made, as well as suggestions for further improvements and expansions.

2 Theory

This section contains a description of relevant theory for the project. After a short introduction about wind velocity, it starts with a general description of airfoils and their parameters, and continues with describing sound and noise. At the end, some theory about CFD software and methods of calculating noise production is included.

2.1 Relative Wind Velocity

A wind turbine is useless without a flow of air, also known as wind, across its wings. The velocity of the wind may be characterised in several ways. For both airplanes, wind turbines and other aerodynamic applications, the relative wind velocity is significantly larger than the experienced wind velocity at standstill (free stream wind velocity). This is due to the object's movement towards the wind direction. The relative wind velocity will as a consequence increase with increasing local radius of a wind turbine blade. For a rotating wind turbine, the relative velocity U_{rel} is given by Equation 2.1, where U is the free stream wind velocity, ω is the angular velocity, r is the local radius and λ is the tip speed ratio relating the tip speed of the wing and the angular velocity of the rotor.

$$U_{rel} = \sqrt{U^2 + (\omega r)^2} = U \cdot \sqrt{1 + \lambda^2} \tag{2.1}$$

The relative velocity can also be characterised relatively to the speed of sound. The Mach number is the dimensionless relation between the relative velocity and the speed of sound c_s. This relation is shown in Equation 2.2.

$$Ma = \frac{U_{rel}}{c_s} \tag{2.2}$$

2.2 Airfoils

An airfoil or aerofoil is the cross sectional shape of a wing. Its front side is called the leading edge and its back is called the trailing edge. The chord length c is the straight line between the leading and trailing edge. A flow of air having the relative wind velocity will under most operating conditions hit the airfoil's leading edge at an angle, namely the angle of attack α, defined as the angle between the relative velocity U_{rel} and the chord length c. All these terms are visualised in Figure 2.1.

2.2.1 Pressure Around Airfoils

The purpose of a wing is to generate lift from an oncoming flow of air or another fluid, having the relative velocity [9]. An airfoil is shaped in a way that makes fluid particles on the top side move faster than those on the bottom side. However, the particles that were separated at the leading edge does not meet at the trailing edge, the top side particles reach the trailing before the bottom side ones, making the velocity difference even larger.

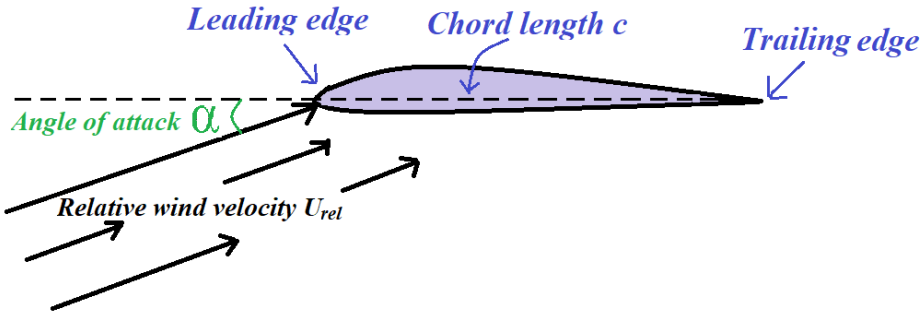

Figure 2.1: Some relevant terms of airfoil geometry and angle of attack α.

According to Bernoulli's principle shown in Equation 2.3, a higher local flow velocity u leads to a lower pressure p on the top side, naming it the suction side. Consequently, the lower flow velocity on the bottom side creates a higher pressure, naming it the pressure side [10]. The parameter ρ in Equation 2.3 is the air density.

$$p + \frac{1}{2}\rho u^2 = \text{constant} \tag{2.3}$$

Pressure around airfoils is often described more in detail than just "suction side" and "pressure side". The pressure coefficient C_p describes the pressure distribution along the whole surface of the airfoil. It is defined in Equation 2.4, where p is the local pressure, p_∞ is the ambient pressure, and U_{rel} is the relative velocity [10].

$$C_p = \frac{p - p_\infty}{\frac{1}{2}\rho U_{rel}^2} = \frac{\text{Static pressure}}{\text{Dynamic pressure}} \tag{2.4}$$

The pressure coefficient is normally plotted as a function of the normalised chord length x/c, which spans from 0 to 1. If the airfoil has a non-symmetrical shape or a non-zero angle of attack, there will be one separate curve for the suction side and one for the pressure side.

2.2.2 Generation of Lift

Pressure differences explained by Bernoulli's principle explain parts of how lift of an airfoil is generated, but it is not the complete physics behind the process. In order to create sufficient lift, airfoils also defect the flow of air downwards at the trailing edge. According to Newton's third law, when the flow of air is pushed downwards, the airfoil is pushed upwards. An airfoil's ability of this deflection is explained by the Coanda effect, which describes a fluid's ability to stick to a surface [11]. The flow on the suction side of will follow the concave surface and deflect downwards, as shown in the first and second case of Figure 2.2. Figure 2.2 also shows that the amount of air deflected increases with increasing angle of attack up to a point where it gets too large. In this case, the flow of air is no longer able to stick to the surface, resulting in strong vortexes and a reduced lift. This case is also referred to as stall.

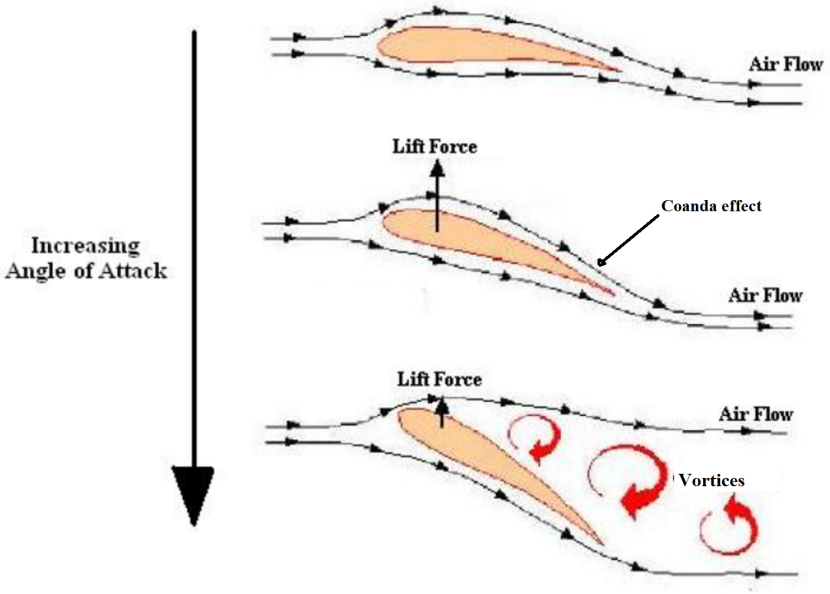

Figure 2.2: At sufficiently large angles of attack, the Coanda effect will contribute to the generation of the lift force. At too large angles of attack, stall and reduced lift will occur. The figure is retrieved from [12].

2.2.3 Airfoil Forces

The lift force is not the only force acting on an airfoil. After passing the airfoil, the flow of air creates vortexes and wakes behind the trailing edge. This especially happens at larger angles of attack, as shown in the last case of Figure 2.2. Such wakes together with friction due to surface roughness creates a drag force, split up into pressure drag and friction drag respectively. Airfoils are constructed with the purpose of creating as much lift and as little drag as possible. Lift force F_l and drag force F_d of two-dimensional airfoils are defined by Equation 2.5 and 2.6 [10].

$$F_l = \frac{1}{2}\rho U_{rel}^2 C_l c \tag{2.5}$$

$$F_d = \frac{1}{2}\rho U_{rel}^2 C_d c \tag{2.6}$$

The C_l and C_d are lift and drag coefficients, and are often plotted as functions of α in order to show properties of airfoils. Such plots are useful for showing the optimal angle of attack at the specific operating conditions.

The lift force F_l is defined as always normal to the relative velocity, while the drag force F_d is defined as parallel with it. The resultant force $\vec{F}$ of $\vec{F_l}$ and $\vec{F_d}$ can be split into a parallel and normal component with respect to the rotor plane. These components are the force $\vec{Q}$, which generates torque, and thrust $\vec{T}$ respectively [13]. This relationship is shown in Figure 2.3.

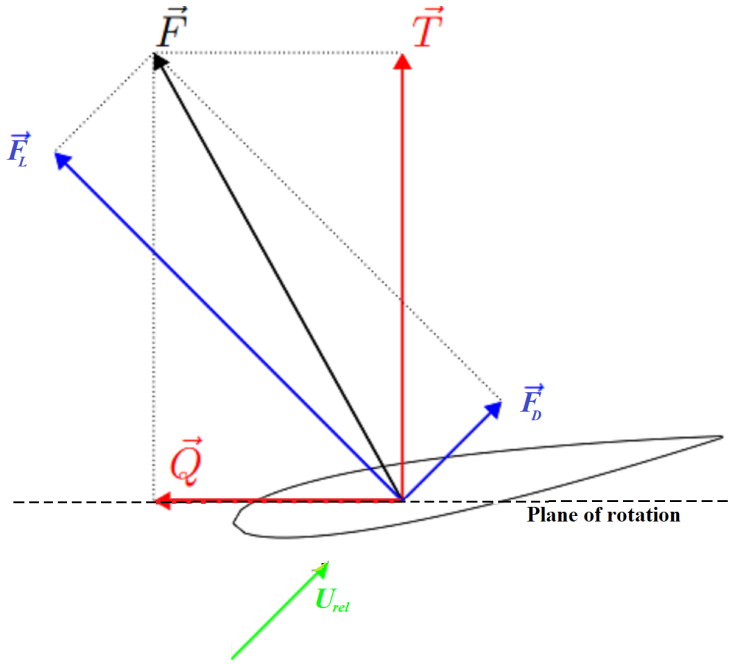

Figure 2.3: Relation between lift F_L, drag F_D, the torque-generating force $\vec{Q}$ and thrust $\vec{T}$. The figure is retrieved from [13].

2.2.4 Boundary Layer

As previously mentioned, one contributor to drag is friction between the object and the flow of air. The area close to the surface where frictional or viscous effects are significant, is called boundary layer (BL). Thickness of the boundary layer of a wind turbine may vary from 1 mm to several tens of cm [10]. The frequently applied "no slip condition" assumes that the fluid sticks to the surface, making the flow velocity zero here [14]. However, when the distance away from the surface increases, the flow velocity increases too, depending on the pressure and viscosity. Figure 2.4 shows an example of flow velocity distribution in a boundary layer.

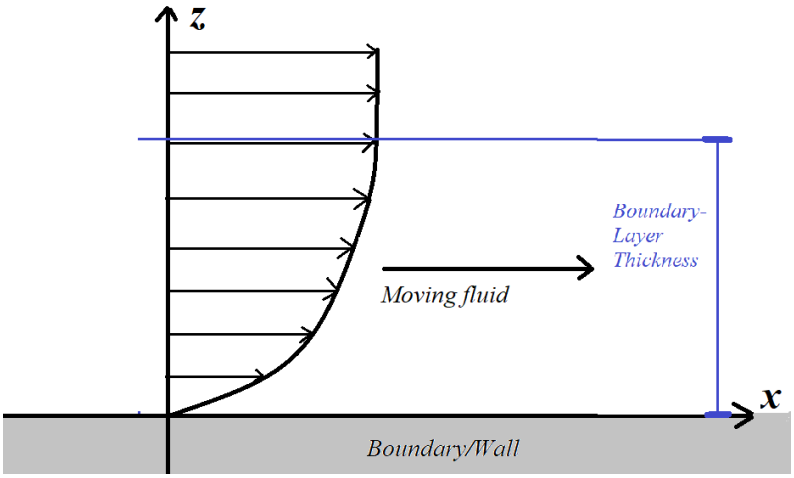

Figure 2.4: A boundary layer at no slip condition. The flow velocity is zero at the surface and increasing further away.

2.2.5 Turbulence and Reynolds Number

The flow in the boundary layer can either be laminar, with smooth and steady streamlines, or it can be turbulent, with irregular and chaotic vortexes. An airfoil usually have a laminar boundary layer at the leading edge, which expands and makes a transition into turbulent towards the trailing edge [10].

Whether a flow is laminar or turbulent depends on many parameters, such as geometry, surface roughness, flow velocity, type of fluid and more [9]. A simple ratio for determining the level of turbulence is the Reynolds number, defined for airfoils in Equation 2.7. The parameter c is the characteristic length, which for airfoils is the chord length, and ν is the kinematic viscosity.

$$Re = \frac{u \cdot c}{\nu} = \frac{\text{Inertial forces}}{\text{Viscous forces}} \tag{2.7}$$

Equation 2.7 shows that if the Reynolds number is kept low, the viscous forces will be larger relative to the inertial forces. These viscous forces is what creates friction drag, and also affecting the velocity and pressure (wake) behind the trailing edge [10]. This means that an increased Reynolds number will reduce the viscous effects, and consequently the impact of wakes. As a consequence, stall occurs on higher angles of attack when Re is higher. High Reynolds numbers also make the viscous forces unable to prevent random fluctuations of the flow, and the flow will become more turbulent [9]. The critical Reynolds value for where a flow transits from laminar to turbulent varies greatly depending on the type of fluid and application.

2.2.6 Airfoil Types

Airfoils can be found in a variety of shapes for use in different applications. There are also a variety of airfoil series, where numerical values represent different characteristics. Two examples are the NACA-series and the DU-series. The NACA0012 airfoil is one of the most documented airfoils, and is often included in scientific studies because many references are available for validating the present method. Two airfoils that are frequently used in wind turbines are NACA64418 and DU96 [1]. The shapes of the three mentioned airfoils are shown in Figure 2.5. As shown in Figure 2.5a, NACA0012 is a symmetrical airfoil, which means that it has the same shape on both the suction and pressure side. Symmetrical airfoils require an $\alpha \neq 0$ to produce any lift. It is noticeable that DU96 in Figure 2.5c has an embedded angle of attack of $4°$, while the NACA profiles have a $0°$ angle of attack. A wind turbine blade usually consists of different airfoils along the wing span, each section optimised for different angles of attack and wind velocity.

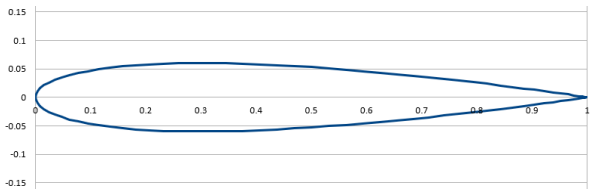

(a) NACA0012

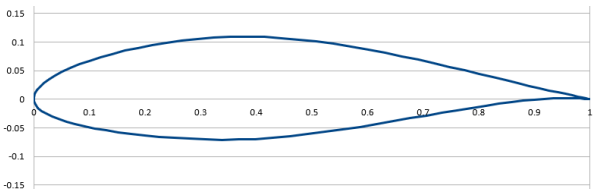

(b) NACA64418

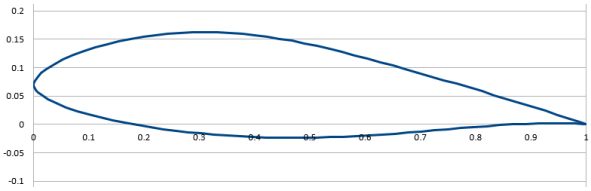

(c) DU96

Figure 2.5: Shape of the well documented NACA0012 and two the two airfoils NACA64418 and DU96, which are frequently used for wind turbines.

2.3 Sound and Noise

The physical definition of sound is vibrations that propagates as waves in a medium. The relationship between wavelength λ, frequency f and the sound velocity c_s is shown in Equation 2.8.

$$c_s = f\lambda \tag{2.8}$$

Octave bands are ranges of sound frequencies covering one octave, meaning that the highest frequency of the range is twice the size of the lowest [15]. For engineering purposes, a fraction of an octave band is often used, such as a "Third octave", which is one third of an octave band [15]. This means that the highest frequency in a third octave band is $\sqrt[3]{2}$ times greater than the lowest. Noise is defined as unwanted sound. This may be a subjective definition, because different people experience different types of noise with unequal levels of annoyance [10]. There are two important terms used for describing sound and noise. The Sound Power Level (or noise pressure level) L_W describes the amount of sound radiated from an object. The Sound Pressure Level (or noise pressure level) L_p is the sound or noise that can be heard at a specific distance from the source [16]. Regulations regarding maximum level of noise pressure level are present in many countries, among others Norway.

Sound is one of the quantities measured with the logarithmic unit decibel (dB). The sound power level in dB is defined mathematically in Equation 2.9, where W is the source sound power and W_0 is a reference sound power, which is usually 10^{-12} W [10].

$$L_W = 10 \log_{10} \frac{W}{W_0} \tag{2.9}$$

The sound pressure level in dB is expressed mathematically in Equation 2.10, where p_s is the instantaneous sound pressure and p_0 is a reference pressure, usually $20 \cdot 10^{-5}$ Pa [10].

$$L_p = 20 \log_{10} \frac{p_s}{p_0} \tag{2.10}$$

2.3.1 Sound Propagation

From Equations 2.9 and 2.10, it can be shown that doubling the sound intensity will give an increase of approximately 3 dB, due to the logarithmic scale. As a consequence, when sound waves spread in three dimensions and the distance from the source is doubled, the area of the wave gets four times larger, and the sound pressure level will decrease by 6 dB [17]. This decrease is the same no matter in which order of magnitude the doubling occurs. However, the propagation of sound or noise over longer distances is much more complicated, and depends on many conditions. Sound waves will be refracted both in the atmosphere, from the ground and from other objects [6]. As a consequence, atmospheric conditions such as wind, humidity, and temperature as well as type of terrain will have an impact on the sound propagation. For example, some studies have shown that the noise may be stronger at night, due to more stable atmospheric conditions [6]. If adding multiple sources of sound, the sound pressure level is not doubled, because of the logarithmic scale. The total sound level from N different sources is calculated by using Equation 2.11 [10].

$$L_{tot} = 10 \log_{10} \sum_{i=1}^{N} 10^{\frac{L_i}{10}} \tag{2.11}$$

2.3.2 Noise Regulations

Many countries have regulations regarding maximum allowed noise pressure levels. In Norway, there is a requirement for maximum allowed level of noise from wind turbines. Heard from the nearest residential area, the noise level has to be below 45 dB, and below 40 dB at night [18]. The owner of the noise creating process (a wind park in this case) is obliged to map the noise production every 5 years to ensure that it follows the guidelines. This noise mapping includes both definition of the type of noise, the sound power and sound pressure level and to evaluate the noise propagation over larger distances, and how it affects the nearest house or cabin [16].

2.3.3 Types of Wind Turbine Noise

There are two categories of noise generated from a wind turbine; mechanical noise from gears and machinery, and aerodynamic noise from the interaction between the blades and the flow of air [6]. On larger commercial wind turbines, aerodynamic noise is by far the most significant, and the one most frequently studied. This aerodynamic noise is again divided into two groups called airfoil self noise and turbulent inflow noise [6]. Turbulent inflow noise is the noise appearing from turbulence in the flow of air that hits the leading edges of the turbine blades. Airfoil self noise is noise generated from turbulence created as the air flows across the surfaces of the airfoils. This self noise consists of several mechanisms, among others trailing edge noise, separation noise and tip vortex noise. Most dominating of these is the trailing edge noise [6]. Most of the airfoil self noise is of the type called Broadband, which is a continuous distribution of sound pressure at frequencies larger than 100 Hz [10].

2.4 Computational Fluid Dynamics (CFD)

In the 1950s and early 1960s, what now would be considered as simple aerodynamic problems were highly challenging. In 1966 however, a breakthrough took place, as researchers were now able to use the developing computational power to solve aerodynamic problems. These techniques and methods quickly evolved into what is now referred to as Computational Fluid Dynamics (CFD) [19]. The core of CFD is to describe both basic differential equations and other advanced equations of fluid dynamics with numbers and numeric calculations. Such calculations often involves thousands, maybe millions of numbers, and extensive CFD calculations therefore relies on the available computational capacity [19]. One application of CFD is to analyse a flow of air across an airfoil.

2.4.1 CFD Software

There are a variety of different CFD software being used for engineering purposes. OpenFOAM is an open-source software package developed by OpenCDF Ltd since 2004 [20]. It is widely applied for many engineering and scientific purposes [21]. OpenFOAM is built upon Linux commands, but also has a Windows version. It contains an extensive library of solvers that aim to solve the Navier-Stokes equations by using different methods with different levels of accuracy [21]. Some solvers are BlockMesh, SimpleFoam and PimpleFoam.

2.4.2 RANS Equations

Simulation of turbulent flows can be challenging, due to the chaotic and three-dimensional nature of turbulent vortexes. One simple and less computational power demanding calculation method applied in engineering is RANS equations (Reynolds Averaged Navier-Stokes Equations) [9]. If several equal experiments with turbulent flows were conducted, a snapshot of the flows would look different for each one. The RANS equations calculate an average in space of these, creating only the larger structures of the turbulence. If the flow is without time variations, it can also be averaged over time [22]. This Reynolds-average is sufficient for calculating forces and other parameters relevant in most engineering purposes. More advanced methods available are LES (Large Eddy Simulation) and DNS (Direct numerical Simulation). DNS is considered as the far most accurate method, but it has a large number of unknown parameters, and therefore requires much more computational power. This level of accuracy is usually unnecessary for most engineering applications [9].

2.4.3 SimpleFoam

An OpenFOAM solver that applies RANS equations is SimpleFoam, which is a steady state solver for incompressible turbulent flows. It applies the SIMPLE algorithm (Semi-Implicit Method for Pressure Linked Equations), which is an iterative method aiming to calculate averaged numerical values for turbulent flows. The core of the algorithm is the incompressible form of the continuity equation and the momentum equation, shown as Equation 2.12 and 2.13 respectively.

$$\nabla \cdot \mathbf{u} = 0 \tag{2.12}$$

$$\nabla \cdot (\mathbf{u} \times \mathbf{u}) - \nabla \cdot \mathbf{R} = -\nabla p_k + S_u \tag{2.13}$$

Here is $\mathbf{u}$ the velocity, p_k is the kinematic pressure, $\mathbf{R}$ is the stress tensor and S_u is the momentum source.

2.5 Simulating Noise Production

Aerodynamic noise around airfoils is generated by turbulence, or local pressure fluctuations in the flow, which can generate sound waves. These pressure fluctuations are either atmospheric (turbulent inflow noise) or being created as the air moves along the airfoil (airfoil self noise). In order to simulate noise production from an airfoil, the distribution of these pressure fluctuations has to be obtained first. This pressure distribution is calculated by using a turbulence model, which solves the RANS equations. Results from the chosen turbulence model can be used as input in one of many possible models for creating the wall-pressure spectrum. Amiet's model uses the wall-pressure spectrum as input to calculate the noise pressure level at a given point.

2.5.1 Spalart-Allmaras Turbulence Model

There is a large variety of turbulence models aiming to solve the RANS equations and in that way calculate pressure fluctuations and other relevant parameters around an airfoil surface. Some turbulence models are the k-ϵ-model, the k-ω-model and the q-ω-model, which are all two-equation models [9]. A single-equation model that can be applied by SimpleFoam is the Spalart-Allmaras Turbulence Model, which is mainly developed for aerodynamic flows. It is based on a transport equation for the eddy viscosity [23]. Parts of the Spalart-Allmaras equation are non-dimensional functions and values, which are regularly calibrated with experimental results for the type of flow the model is aiming to reproduce [23]. This makes the model more reliable and frequently applied.

2.5.2 Wall-Pressure Spectrum

A wall-pressure is produced by velocity fluctuations in a turbulent boundary layer as the air flows across the surface of an airfoil [24]. Aerodynamic noise around airfoils is generated by these wall-pressure distributions. The fluctuating wall-pressure causes vibrations and noise, and is scattered and diffracted by the sharp trailing edge, which makes the turbulent kinetic energy

convert into acoustic energy in the form of trailing edge noise [25]. In addition, the boundary layer is increasing in size and turbulence level towards the trailing edge of an airfoil. Therefore, the trailing edge boundary layer is of particular interest when studying the most significant noise production form an airfoil. The noise from the wall-pressure is usually presented as a wall-pressure spectrum, which is a plot showing the sound level ϕ_{pp} as function of frequency f. There are many different models for calculating the wall-pressure spectrum from a pressure distribution, and they use different scaling factors, as there are no universal standard. Some examples are "Lee's model" [26], which is an extension of the "Rozenberg's model" [24], "Goody's model", "Catlett's model", "Kamaruzzaman's model" and the "Hu & Herr model" [1].

2.5.3 Amiet's Model

Amiet's model is maybe the most widely used model for calculating the noise produced by airfoils and wind turbines. The wall-pressure spectra are used as input in Amiet's theory for airfoil noise, in order to calculate the noise pressure level at a given point. Amiet's theory was developed by R. K. Amiet in the 1970s. It assumes that the inflow turbulence variations of an airfoil are small and unchanged compared to the flow velocity, and that the air is inviscid when interacting with the surface [25]. It connects the surface pressure fluctuation spectrum to the acoustic pressure distribution [6]. The airfoil is further modelled as a flat plate with no thickness and an infinite span length [25]. A radiated sound field is calculated with an assumption of a constant, or "frozen" turbulence at the trailing edge [1].

3 Methodology

The project's methodology is described in detail in this section. In short, the work consisted of creating and modifying a simulation model into making correct results for lift, drag and a pressure distribution around three airfoils, and use the results from this model to simulate noise production. Intermediate results from this work were validated against references from literature in order to ensure that the results had acceptable reliability. The whole methodology was conducted for three different airfoils; NACA0012, NACA64418 and DU96. Their shapes are shown in Figure 2.5 in the Theory, with the NACA profiles having a 0° angle of attack and DU96 having a 4° angle of attack. The methodology is similar to the one described by Sintef, IVKDF and some other institutions as part of the EU founded UPWARDS 2020 project [1], but uses a different software (OpenFOAM) and some other alternative steps.

3.1 Software Setup

The OpenFOAM solver SimpleFoam was used for calculating relevant parameters for the airfoils in this project. It required among others a "BlockMeshDict" file representing the airfoil shape. Program files and their setup are based upon an online tutorial, but with some additional code provided by Sintef. The type of simulations performed in this study can be difficult to visualise without any tools, so ParaView was used for this purpose. ParaView is an open-source application which allows simple visualisations by reading, filtering and rendering of data sets in two or three dimensions [27]. It has a large variety of filters that can be applied to a model to visualise relevant parameters and results.

3.1.1 BlockMesh: Airfoil Geometry

The three different airfoils required their own BlockMeshDict file containing their geometry with a fine-masked "grid" of cells around. In each cell, pressure, wind velocity and other relevant parameters could be calculated. A "BlockMeshDictGenerator" from Thien Phan's website [28] was used for generating the BlockMeshDict files. It allowed to enter airfoil coordinates provided by IVKDF into an Excel sheet that converted the entered parameters into a BlockMeshDict file. It was however necessary to scale and modify the airfoil coordinates so that they went exactly from $x = 0$ to $x = 1$ and thus fitted in the Excel formulas. The provided coordinates of the two NACA profiles gave them an initial angle of attack of 0°, while the coordinates for the DU96 gave an initial value of 4° angle of attack.

It was also necessary to ensure that the mesh size was large enough to produce accurate results. In order to achieve this, several parameters in the BlockMeshDictGenerator were changed from the default ones. Several combinations were tried until acceptable results for lift and drag coefficients (described later) where obtained. Table 3.1 shows the values of these size parameters, which were the same for all three airfoils.

Table 3.1: Size parameters used in the the BlockMeshDict generator from [28].

Parameter	Value
Distance to inlet (chord lengths)	12
Distance to outlet (chord lengths)	20
Angle of response (°)	0
Cell size at leading edge	0.01
Cell size at trailing edge	0.01
Cell size in middle	0.01
Separating point position (fraction of chord length)	0.4
Boundary layer thickness	2
First layer thickness	0.005
Expansion ratio	1.2
Max cell size in inlet	0.02
Max cell size in outlet	0.02
Max cell size in inlet x outlet	0.02
Number of mesh on boundary layer	42
Number of mesh out of boundary layer	101
Number of mesh at tail	148
Number of mesh in leading	81
Number of mesh in trailing	160

Some parameters in Table 3.1 need explanation. The distances to inlet/outlet is how large the total mesh is relative to the airfoil. Angle of response is the angle of a strip with finer grid behind the trailing edge. First layer thickness is the thickness of the first cell on the surface of the airfoils, and the expansion ratio says how much larger the next ones are. The boundary layer thickness of 2 is just where the mesh has the "boundary layer geometry", and explains nothing about the actual thickness of the boundary layer during simulation. The same is the case for the separation point. Max cell size is set low to keep the grid fine, as well as there are large numbers of meshes in the last rows of the table.

When running the "blockMesh.exe" command in OpenFOAM, the BlockMesh was created, and Figure 3.1 shows the ParaView visualisation of the BlockMesh for each airfoil. DU96 already have an initial 4° angle of attack from the coordinate axes, while the NACA profiles have $\alpha = 0°$. As seen in Figure 3.1, the cell size is significantly smaller closer to the airfoil surface, where the boundary layer is located. A larger cell size further away from the airfoils is acceptable, since the flow here will be nearly undisturbed. It is then possible to simulate the turbulence with a high degree of accuracy without having very power demanding for calculations of nearly undisturbed flows. Figure 3.1 also shows a higher resolution right behind the trailing edge than further away from it.

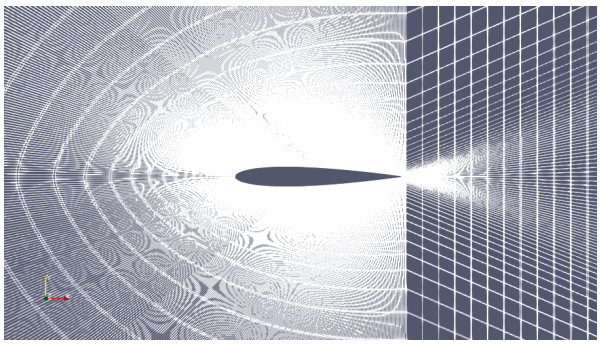

(a) NACA0012

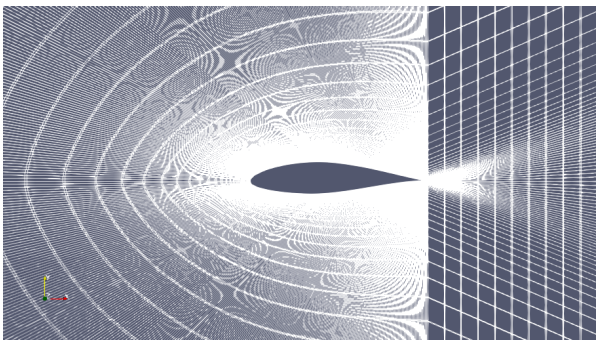

(b) NACA64418

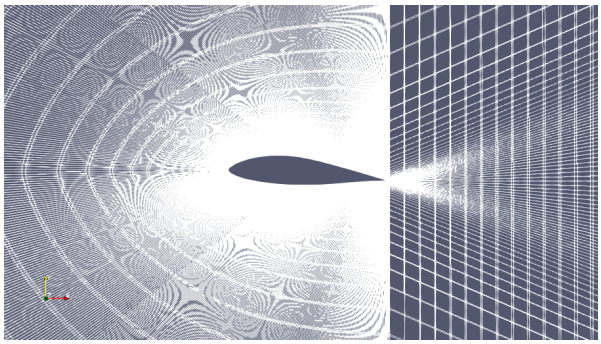

(c) DU96

Figure 3.1: BlockMeshes of the three airfoils, visualised in ParaView.

However, the BlockMeshDictGenerator was configured in a way making the cell size downstream of the trailing edge significantly larger and therefore more inaccurate than the cell size around the rest of the airfoil, as shown in Figure 3.1. A zoomed in version of the mesh size at the trailing edge of NACA0012 is shown in Figure 3.2, and shows the same. The other airfoils have similar trailing edge meshes. This aspect turned out to create inaccurate noise results. However, it was unfortunately discovered so late in the project that it was not enough time to improve the meshes.

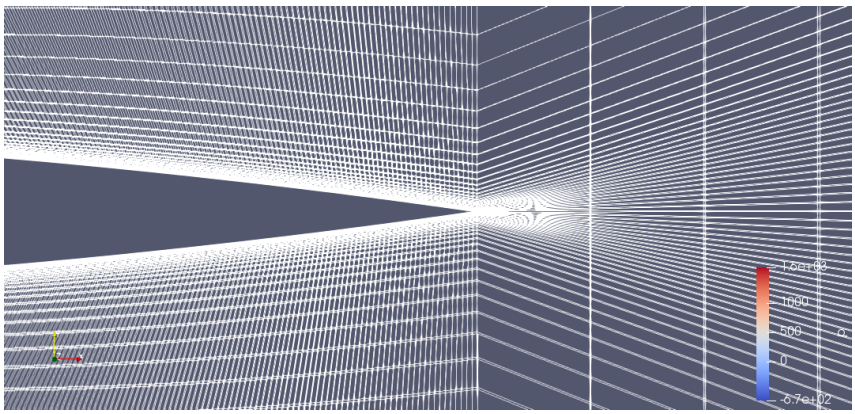

Figure 3.2: A zoomed in view of the mesh at the trailing edge of NACA0012. The cell size is significantly larger downstream of the trailing edge than upstream. The other airfoils have similar trailing edge meshes.

3.1.2 SimpleFoam: Pressure Distribution

After producing the BlockMeshes, the RANS equation based SimpleFoam solver in OpenFOAM was applied. The simulation model and its settings were based upon an OpenFOAM tutorial [29]. SimpleFoam applied the Spalart-Allmaras turbulence model to simulate air flows and pressure differences along the surfaces of the airfoils. The setup also included some additional configurations provided by Sintef which calculated lift and drag coefficients, as well as the pressure coefficient along the surfaces. Physical constants and parameters from the Sintef and IVKDF document [1] were applied so that their results could be used as a reference during parts of the validation. These values were typed into their respective code files belonging to the SimpleFoam solver, and are shown in in Table 3.2. The Reynolds number is calculated by using Equation 2.7, and the Mach number is calculated by using Equation 2.2. Some of the other physical parameters are slightly modified to an operating condition with a round Reynolds number that is easier to compare with references. The table shows different chord lengths, but the same span length for the three airfoils, and this had to be included in their respective BlockMeshDict files. An "endTime" for the iteration was set to 500. Many of the calculations converged after 500 iterations, and the rest had negligible changes when more iterations were run.

Table 3.2: Physical constants and parameters applied to in SimpleFoam solver. They are the same as in [1].

Parameter	NACA0012	NACA64418	DU96
Free stream velocity U_∞ [m/s]	56	62	60
Density ρ_∞ [kg/m^3]	1.181	1.181	1.164
Kinematic viscosity ν [m^2/s]	$1.4933 \cdot 10^5$	$1.488 \cdot 10^5$	$1.593 \cdot 10^5$
Reynolds number Re [-]	$1.5 \cdot 10^6$	$2.5 \cdot 10^6$	$1.13 \cdot 10^6$
Mach number Ma [-]	0.1664	0.183	0.173
Angle of attack α [°]	0	0	4
Chord length c [m]	0.4	0.6	0.3
Span length l [m]	1	1	1

3.2 Validation

The SimpleFoam solver calculated values for lift coefficient C_l, drag coefficient C_d, pressure coefficient C_p and many other less relevant parameters for the airfoils. Before advancing to the noise calculations, these results were validated against references to ensure acceptable accuracy. When necessary, some input parameters were changed and the simulations were run again until acceptable results were produced.

3.2.1 Lift and Drag Coefficients

Airfoils are often characterised in literature by plots of lift and drag coefficients as functions of angle of attack. Therefore, the SimpleFoam solver was run for different α-values for each airfoil, and the coefficient values from the last iteration step were saved for each case. These data were plotted in the same figures as experimental reference results collected from different sources. It was important that the reference values were for approximately the same Reynolds numbers as the results from this study, as lift and drag is dependant on the Re value. The online tool WebPlotDigitizer [30] was used to read values from other literature's plots, and Matlab was used for plotting C_l, C_d and C_p curves for this report.

When changing the value of α for each simulation, values for incoming flow velocity and direction of lift and drag had to be changed. The coordinate system was aligned with the meshes and chord lengths of NACA0012 and NACA64418, and had a 4° angle with the chord length of DU96. This was included already in the airfoil coordinates provided by IVKDF, to make the same OpenFOAM setup work for the NACA profiles at 0° and the DU96 at 4°. It was necessary to decompose both U_{rel}, F_l and F_d into their respective parallel and normal components with respect to the chord length plane. Since the geometry file for the DU96 airfoil already have a 4° angle of attack from the coordinate system, the same values for lift and drag directions will correspond to different angles of attack for DU96 than for the NACA-airfoils. The decomposition was done by multiplying the U_{rel} from table 3.2 or the value 1 for each force component with either $\sin\alpha$ or $\cos\alpha$ in accordance with simple trigonometric identities. Wind velocity was modified by changing the coordinates of the "internalField" in the "U" file in the "0" folder. Directions of lift and drag were modified by changing the "liftDir" and "dragDir" coordinates in the "controlDict" file located in the "system" folder.

3.2.2 Pressure Coefficient

The SimpleFoam solver also calculated the pressure coefficient C_p along the surfaces of the airfoils. This was only done for one selected angle of attack; 0° for the NACA profiles and 4° for the DU96 airfoil, in accordance with the work of Sintef and IVKDF [1]. Since the corresponding geometry coordinates did not accompany the C_p data from SimpleFoam, the C_p-curves were created using ParaView's "Plot On Intersection Curves" filter. Its plane was oriented parallel with the airfoil mesh, and in the middle of its thickness. In addition, the origin was placed somewhere inside the airfoil at the chord length. This means that the origin was located in $(x, y, z) = (0.25, 0, 0.5)$ and the plane's normal vector was $(x, y, z) = (0, 0, 1)$. These settings made the airfoil surfaces correspond to the intersection curves. Table values for the generated plots in ParaView for the last iteration step were retrieved and used to make C_p curves for the three airfoils. These were also compared to references with approximately the same Reynolds numbers in the same way as the lift and drag coefficients.

3.3 Noise Calculations

After creating pressure distributions with acceptable agreement with reference values, the completed pressure distributions were sent to IVKDF for running noise simulations around the airfoils. All these calculations were performed in Python, and following the same methods as Sintef and IVKDF used in the UPWARDS project [1]. The pressure distribution calculated with SimpleFoam was used as input in Lee's model [26] for creating the wall-pressure spectra near the trailing edge of the airfoils. All acoustic results were produced at a 1 m distance from the trailing edge in the direction normal to the chord length, as shown in Figure 3.3, retrieved from [1].

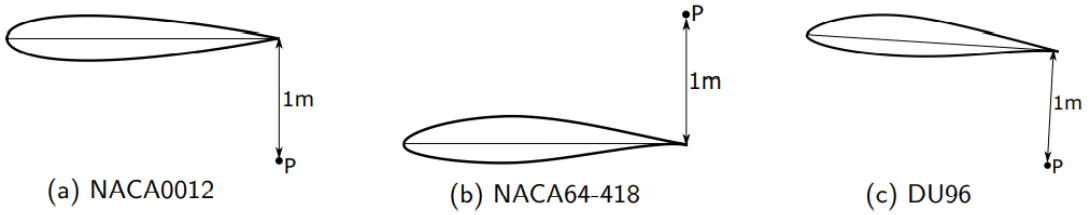

Figure 3.3: The location where the acoustic results are calculated: 1 m away from the trailing edges in the normal direction with respect to the chord length. The figure is retrieved from [1].

The trailing edge is where the boundary layer is both most turbulent and scatters the wall-pressure distribution, generating the main contributor of aerodynamic noise. It is therefore the most relevant location to study the noise production. It would of course be possible to place the point P somewhere else. In the last step, Amiet's model was applied to produce third octave band representations of the sound pressure levels $L_{p(1/3)}$ at the same points located 1 m away from the trailing edge. These plots were also validated against the literature where available, and possible deviations were discussed.

4 Results

All results from the project are presented in this section. The first subsection contains the C_l and C_d vs. α curves, ehile the second contains the pressure distributions, shown as C_p vs. x/c curves. The plots of the coefficients also include experimental reference data for validating this study's results. In the last subsection, results from the noise simulations run by IVKDF are presented.

4.1 Lift and Drag Coefficients

Values for lift and drag coefficients were obtained for several α-values in steps of 5° with some exceptions. The plots also include reference values for the same Reynolds number, or as close as possible when the exact same was not available.

4.1.1 NACA0012

The C_l-α and C_d-α curves for NACA0012 are shown in Figure 4.1. These figures also contain curves representing reference data for a slightly lower and higher Reynolds number than the results, represented by a blue and light blue curve respectively. The reference for $Re = 1 \cdot 10^6$ are experimental data retrieved from [31] and the reference for $Re = 2 \cdot 10^6$ are also experimental data retrieved from [32]. It can be expected that the curve of this study, with a Reynolds number of $1.5 \cdot 10^6$, should be between these reference values.

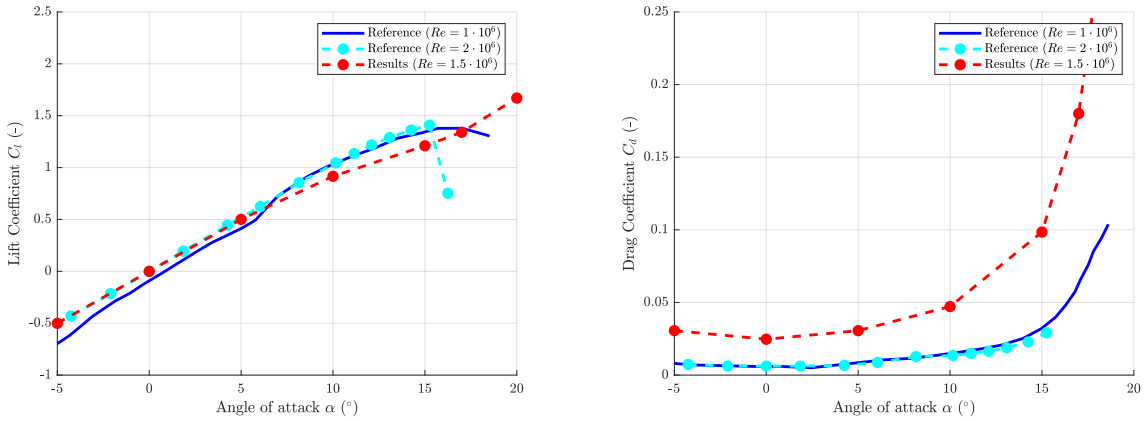

(a) Lift coefficient C_l VS. α.

(b) Drag coefficient C_d VS. α.

Figure 4.1: Lift and drag coefficients for NACA0012 at $Re = 1.5 \cdot 10^6$. Experimental reference values for $Re = 1 \cdot 10^6$ are retrieved from [31], and values for $Re = 2 \cdot 10^6$ are retrieved from [32].

4.1.2 NACA64418

The C_l-α and C_d-α curves for NACA64418 are plotted in Figure 4.2. These figures also contain blue and light blue curves representing experimental reference data. Lift data for both Reynolds numbers are retrieved from [33] and drag data are retrieved from [34]. Reference values for C_l

were only available at Reynolds numbers $1 \cdot 10^6$ and $6 \cdot 10^6$, but it can be assumed that this study's Reynolds number of $2.5 \cdot 10^6$ will be somewhere between. For C_d, only reference values for $Re = 6 \cdot 10^6$ were available.

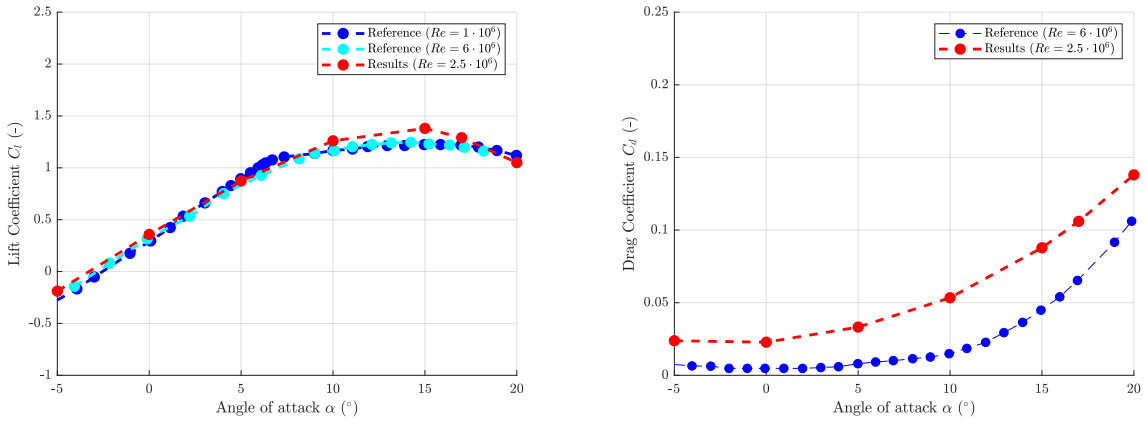

(a) Lift coefficient C_l VS. α.

(b) Drag coefficient C_d VS. α.

Figure 4.2: Lift and drag coefficients for the NACA64418 airfoil at $Re = 2.5 \cdot 10^6$. Reference values for C_l are retrieved from [33], and for C_d are retrieved from [34].

4.1.3 DU96

The C_l-α and C_d-α curves for DU96 are plotted in Figure 4.3. These figures also contain blue curves representing experimental reference data retrieved from [35]. Lift coefficient data were only available for $Re = 1 \cdot 10^6$, which is slightly different from this study's Reynolds number of $1.13 \cdot 10^6$. Reference data for the drag coefficient were only available for $Re = 0.7 \cdot 10^6$, so some deviation here can be expected.

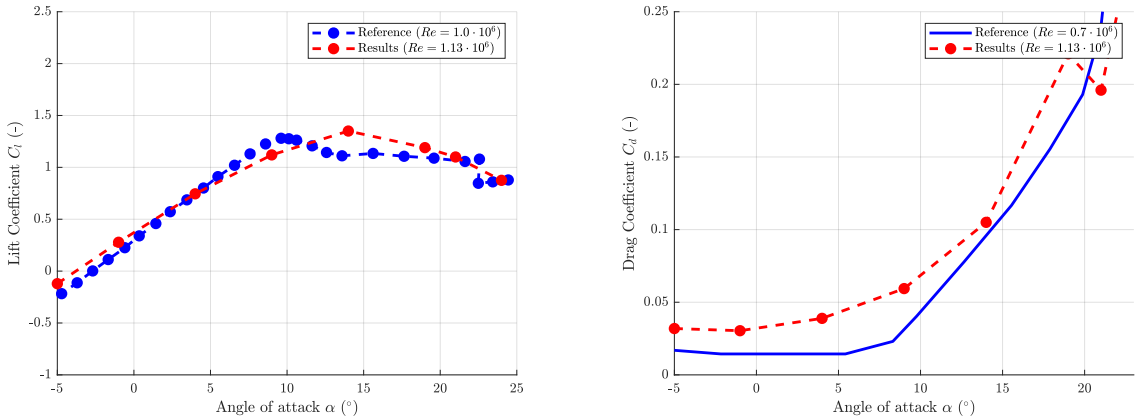

(a) Lift coefficient C_l VS. α.

(b) Drag coefficient C_d VS. α.

Figure 4.3: Lift and drag coefficient values for DU96 at $Re = 1.13 \cdot 10^6$. Experimental reference data are retrieved from [35].

4.2 Pressure Coefficient C_p

The pressure distributions are presented as C_p vs. x/c curves. They are only included for $\alpha = 0°$ for the NACA airfoils and $\alpha = 4°$ for the DU96 airfoil, in accordance with the work of Sintef and IVKDF [1]. Reference values from literature are included for validation.

4.2.1 NACA0012

The C_p distribution along NACA0012 for $\alpha = 0°$ and $Re = 1.5 \cdot 10^6$ is plotted in Figure 4.4. The reference data in the blue curve are retrieved from [1] by Sintef and IVKDF, and should ideally be in good accordance with this project's results, since this study's methodology has followed their setup. Since NACA0012 is a symmetrical airfoil and $\alpha = 0°$, the C_p curves for the pressure and suction side are overlapping.

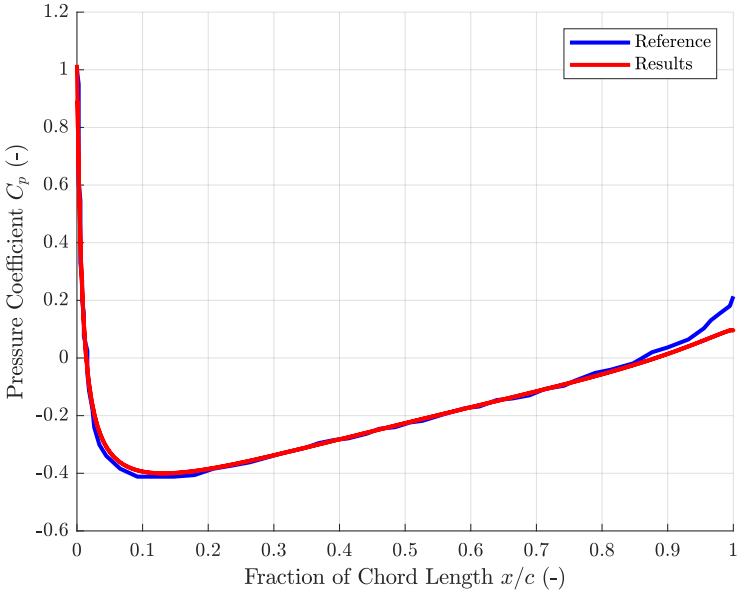

Figure 4.4: Pressure coefficient C_p along the surface of NACA0012 at $Re = 1.5 \cdot 10^6$ and $\alpha = 0°$. Reference values are retrieved from [1], provided by Sintef and IVKDF.

4.2.2 NACA64418

The C_p distribution along NACA64418 for $\alpha = 0°$ and $Re = 2.5 \cdot 10^6$ is plotted in Figure 4.5. Reference values for this airfoil at the same Reynolds number were not available. However, one computed data set for $Re = 6 \cdot 10^6$ was available from [36]. Some deviation may be expected because of this difference.

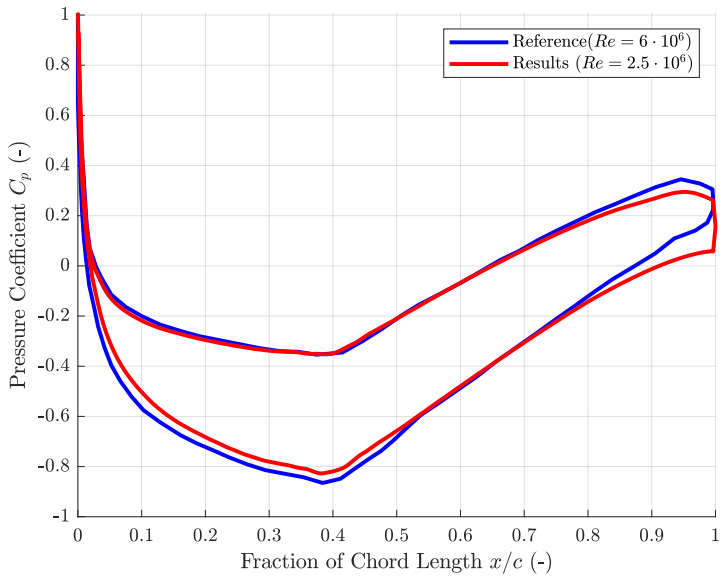

Figure 4.5: Pressure coefficient C_p along the surface of NACA64418 at $\alpha = 0°$ and $Re = 2.5 \cdot 10^6$. Computed reference data are retrieved from [36].

4.2.3 DU96

The C_p distribution along DU96 for $\alpha = 4°$ and $Re = 1.13 \cdot 10^6$ is plotted in Figure 4.6. The reference data are retrieved from the work of Sintef and IVKDF [1]. As for NACA0012, they should ideally be in good accordance with this project's results, since the methodologies follows the same setup. Since DU96 is plotted with a larger angle of attack than the NACA profiles, a larger difference between the pressure side and suction side can be observed.

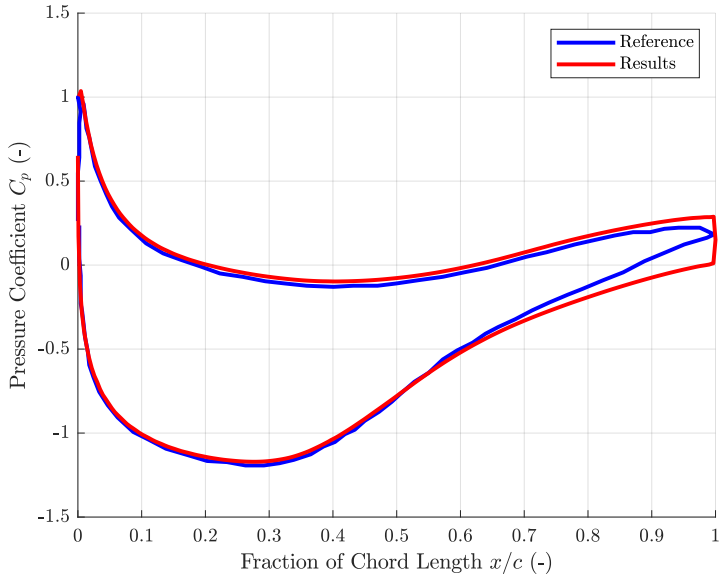

Figure 4.6: Pressure coefficient C_p along the surface of DU96 at $Re = 1.13 \cdot 10^6$ and $\alpha = 4°$. Reference values are retrieved from [1] provided by Sintef and IVKDF.

4.3 Noise Results

Results from the noise calculations performed in Python by IVKDF are presented in this subsection. These include the wall-pressure spectra and the sound pressure level, both calculated at the point 1 m away from the trailing edges, in accordance with Figure 3.3. These plots also include the same experimental reference data that were used by Sintef and IVKDF, which are retrieved from [37].

4.3.1 Wall-Pressure Spectra

Figure 4.7 shows the wall-pressure spectra of each airfoil, represented by ϕ_{pp} as a function of frequency f. They are calculated 1 m away from the trailing edges, by using Lee's model. The red curve is the suction side (SS) and green is the pressure side (PS), and they are overlapping for NACA0012. The black curves are reference data retrieved from [37]. No appropriate reference was available for DU96.

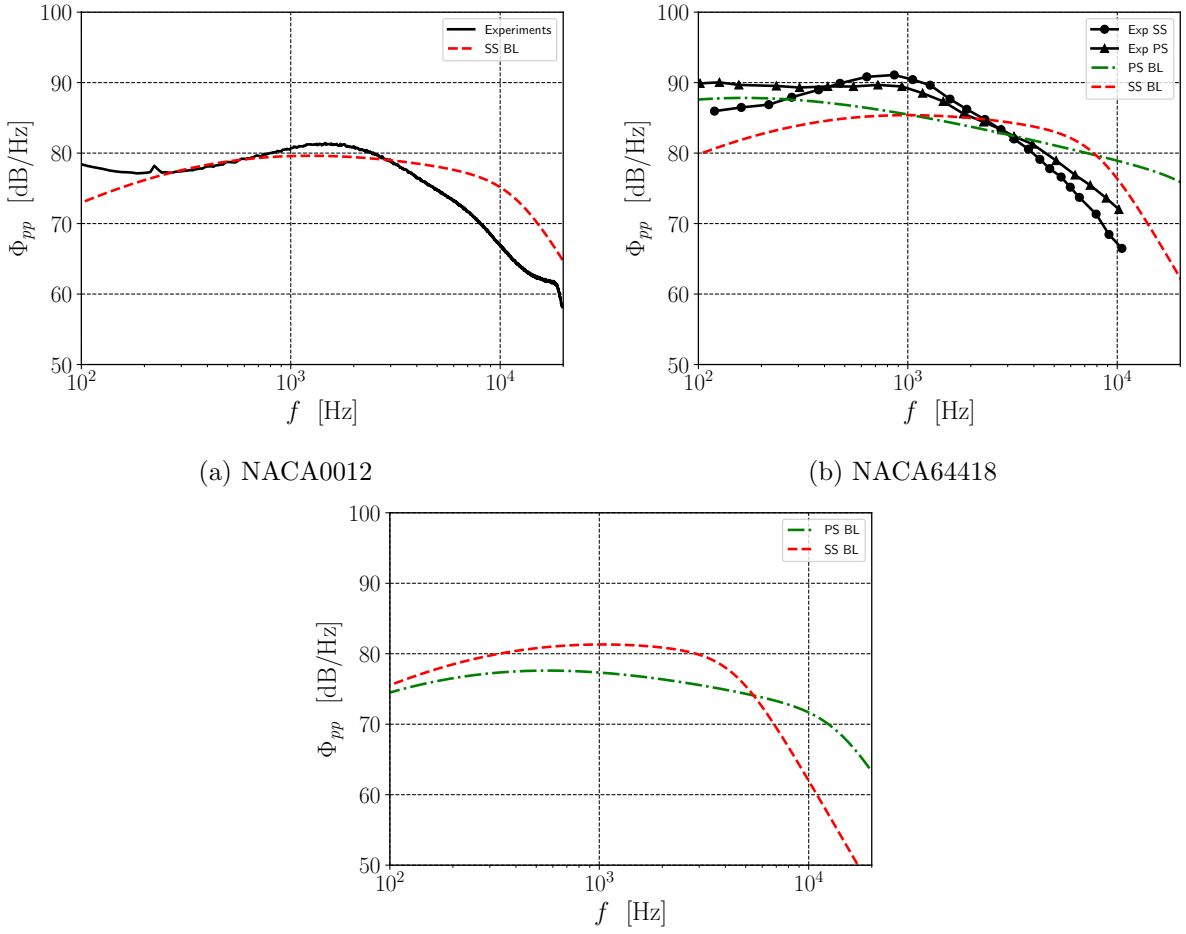

(a) NACA0012

(b) NACA64418

(c) DU96

Figure 4.7: Wall-pressure spectra 1 m away from the trailing edges in the normal direction with respect to the chord length. The black curves are reference data retrieved from [37].

4.3.2 Sound Pressure Levels

Figure 4.8 shows the sound pressure levels at 1 m distance from the trailing edges of the three airfoils. The plots show a third octave band representation of L_p, meaning that the sound levels are ordered into frequency ranges at a width of $\frac{1}{3}$ octave. The values are calculated by using Amiet's model with the wall-pressure spectra as input. The blue curves show the total noise levels from both the pressure and suction side contribution. The black curves are reference data retrieved from [37].

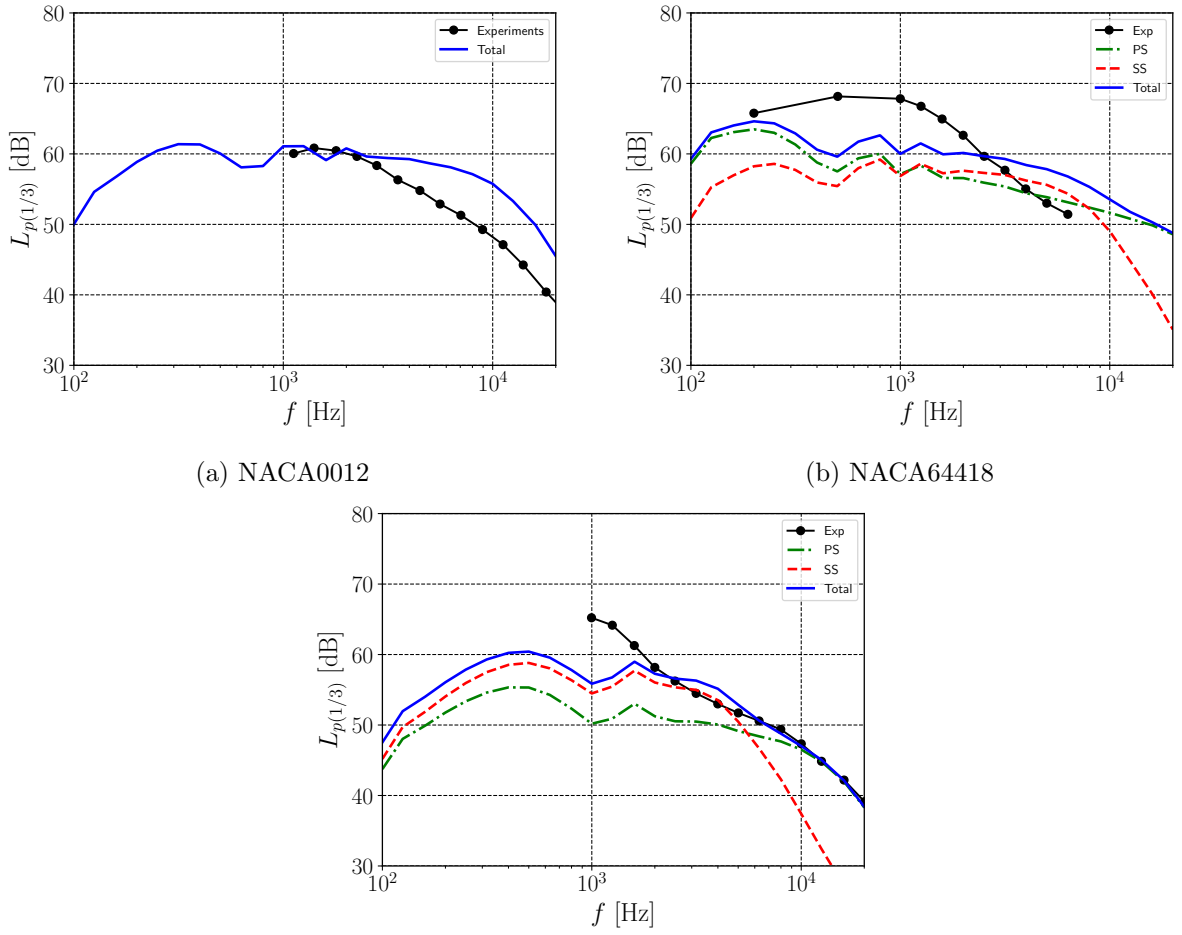

(a) NACA0012

(b) NACA64418

(c) DU96

Figure 4.8: Third octave band representation of sound pressure levels L_p. The black curves are reference data retrieved from [37].

5 Discussion

This section contains a discussion of the results. A significant part of the study was to validate the OpenFOAM methodology and the noise results against references, so a large part of the discussion will be around whether the results are in agreement with references or not, and what the reasons for deviations may be. In the last two subsections, aspects regarding validity and further work are discussed.

5.1 Validation of Lift, Drag and Pressure Coefficients

Figures 4.1a, 4.2a and 4.3a show that the lift coefficients calculated in this study are generally in good agreement with their corresponding references, especially for angles of attack lower than 10°. For higher α-values, there are however some deviations. NACA0012's lift coefficient in Figure 4.1a is slightly lower than both its references at large α. In addition, the value of C_l continues to increase up to 20°. This is where stall and reduced lift usually occurs, as also suggested by the references, which starts to decrease around 15-17°. More calculations on higher angles of attack could have been performed to study this further. However, this suggests a limitation in the application area of the present model.

Results for NACA64418 in Figure 4.2a and DU96 in Figure 4.3a show a slightly higher value of C_l than the references around $\alpha = 15°$, before they are in good agreement at even higher angles of attack. For the DU96 case, some of the deviation may be explained by a slight difference in Reynolds number between results and reference ($1.13 \cdot 10^6$ vs. $1.0 \cdot 10^6$), since the lift coefficient is dependant on the Reynolds number. However, the two different Reynolds numbers in the references for NACA0012 and NACA64418 have negligible differences between them, so the small difference in Reynolds number for DU96 is less likely to have a significant impact on the deviation.

Figures 4.1b, 4.2b and 4.3b show that the calculated drag coefficients are significantly higher than the references for all three airfoils. The largest deviations are for the NACA profiles in Figures 4.1b and 4.2b. The two reference Reynolds numbers for NACA0012 are merely overlapping, but still significantly lower than the obtained results. For DU96 in Figure 4.3b, the deviation from the reference is lower, but still significant. This may partly be explained by the fact that the reference is from a different Reynolds number ($0.7 \cdot 10^6$ vs. $1.13 \cdot 10^6$). A lower Reynolds number gives a higher drag, and hence a smaller deviation in this case. However, as for C_l, the two different reference Reynolds numbers for NACA0012 in Figure 4.1b suggests that even larger relative differences in Reynolds number have little impact on the C_d curve.

The pressure distributions were presented as C_p curves in Figures 4.4 through 4.6. All three cases show fairly good agreement with their references. The only exception is closer to the trailing edge, where the results for all three airfoils deviate significantly from their references. The C_p curves for the pressure and suction side of NACA0012 are overlapping, since NACA0012 is a symmetrical airfoil with $\alpha = 0°$. DU96 has a larger gap between the pressure and suction side curves due to a higher angle of attack than the other airfoils. For NACA64418, the reference has a Reynolds number significantly different from the one used in this study. Since the other two airfoils are compared directly with the work of Sintef and IVKDF, a larger deviation of the NACA64418 deviation may be expected. This may explain a small deviation in on the suction side of NACA64418, shown in Figure 4.5.

5.2 Trailing Edge Mesh

An explanation of the deviation in C_p towards the trailing edge is the shape and size of the BlockMesh. Figure 3.1 shows that while the meshes are fine at the leading edge and middle of the airfoil, they get significantly coarser behind the trailing edge. The zoomed in version in Figure 3.2 shows it more clearly; the width of the cells after the trailing edge is large compared to the rest of the mesh. This fact was discovered late in the project, and there was not enough time to improve the meshes. It can explain why the C_p curves are in such good agreement along the whole chord length, where the mesh is fine, except at the trailing edge, where the mesh is more coarse. The good agreement for the rest of the airfoil suggests that nothing is directly wrong with neither the BlockMesh or the calculation methods, the BlockMesh is just inaccurate at the trailing edge. A finer mesh at the trailing edge would most likely reduce the deviations in C_p significantly.

The inaccuracy of the trailing edge mesh can also explain why the drag values are higher than their references. A contributor to the drag force are wakes and vortexes behind the trailing edge, which are now being inaccurately modelled. Considering the C_p curve of NACA0012 in Figure 4.4, the results show a lower C_p than the reference close to the trailing edge. A lower pressure than expected will result in a larger drag force from the wakes behind the airfoil. NACA64418 has also a lower C_p than its reference, according to Figure 4.5, resulting in a too high C_d-value. The same conclusion can also be drawn for DU96. Figure 4.6 shows that the C_p is lower than the reference on the suction side, but slightly higher than the reference on the pressure side. However, the difference on the suction side is larger, making a net lower C_p at the trailing edge than the reference suggests. As a result, the drag coefficient is higher than its reference. Still, the deviation in drag for DU96 is less than for the NACA airfoils, which may be explained by the smaller net deviation in C_p for DU96. 4.3b.

5.3 Pressure Calculation Methods

The SimpleFoam CFD solver that was applied in this project is based on RANS equations. This is a less accurate and less computational power demanding method used in CFD simulations. In addition, the mesh around the airfoils were coarser, and the iteration time shorter, than most similar studies [1], [6], [36]. This made each simulation take less than 10 minutes on a simple laptop with an i3 processor, but may have caused some inaccuracies in the results. A finer mesh and larger iteration time might have shifted some values slightly, making them closer to reference ones. Changes of this character can easily be applied to the methodology. Another possibility is to apply DNS or LES simulations instead of RANS equations. However, the detailed turbulence modelling in methods are usually not necessary for calculating overall force parameters of a whole airfoil. It is not necessary to know all fluctuations of C_p over both time and space, the average is usually sufficient for creating a C_p curve that can be validated.

5.4 Wall-Pressure Spectra and Sound Pressure Levels

The wall-pressure spectra presented in Figure 4.7 were calculated 1 m away from the trailing edges normal to the chord lengths. This is where the meshes were least accurate, as discussed in subsection 5.2. As a consequence, they show some deviations from their references, and some of this is most likely explained by the inaccurate mesh. However, the resulting wall-pressure curve for NACA0012 in Figure 4.7a is nearly overlapping its reference for a large range of logarithmic frequencies around 10^3 Hz. For NACA64418 in Figure 4.7b, the deviation is larger, as the methodology seems to underestimate the wall-pressure at low frequencies and overestimate on higher frequencies. The sound pressure levels of the airfoils in third octave band representations were shown in Figure 4.8, and the shapes of the curves are similar to those of the wall-pressure spectra. Therefore, they show many of the same deviations from their references. There was also an available reference for DU96's sound pressure level in Figure 4.8c, showing that the results for this airfoil are in good agreement at high frequencies, but underestimates at medium frequencies.

An additional source of inaccuracy in the noise results, in addition to the coarse trailing edge mesh, is the applied models for calculating the wall-pressure spectra and sound pressure level. The work by Sintef and IVKDF [1] found that Amiet's model gave less accurate results for the less flat NACA64418 airfoil. Amiet's model assumes flat plate boundary layers, and NACA0012 is significantly more "flat" than the other airfoils. This may explain why the wall-pressure spectra is in better agreement at some frequencies for NACA0012 than for the other airfoils. However, the work by Sintef and IVKDF [1] also had some deviations between their results and the same references as presented here. Some of their deviations were smaller than obtained in this study, and some were approximately the same size. The present methodology is therefore not necessarily less accurate than the one presented in [1], especially not if the meshes in this are improved to be finer at the trailing edge. Both studies show however, that simulating aerodynamic noise from airfoils with high accuracy is challenging.

5.5 Area of Validity

Results and methodology from this study can be applied for other purposes regarding studies of airfoils. The lift and drag curves are calculated for some of the higher, but still representative Reynolds numbers for large wind turbines. Those plots with references at different Reynolds numbers have also shown that even higher Re values most likely have little impact on the C_l and C_d values, especially at low angles of attack. The C_p curves of the NACA airfoils were calculated for $\alpha = 0°$ in this study. This may have a more limited area of usage, since this case produces no lift for NACA0012, and only a small lift for NACA64418. For DU96 at $\alpha = 4°$, a significant, but not optimal lift is generated, making the area of usage slightly larger. The same is case for the noise calculations, which are also calculated for $\alpha = 0°$ and $\alpha = 4°$ respectively. However, even though $\alpha = 0°$ does not produce much lift, this case can still occur for sections of a wind turbine wing under normal operating condition. It is therefore relevant to study the noise production here too, as well as for stall angles of attack, as they can also be present for sections of a wind turbine wing during normal operation. As discussed in the next subsection, the methodology of this study can easily be repeated for other, more relevant operating conditions.

The simulations in this study were conducted with chord lengths of less than 1 m, according to Table 3.2. However, the noise results can still be representative for larger airfoils. The results depend on the Reynolds number, and by changing one of the parameters in Equation 2.7, for example chord length c, other parameters, such as wind velocity can be changed in the opposite direction, making the Re value stay the same. The same Reynolds number should give the same noise results, independent of the airfoil size. It is however not investigated whether the applied methodology is valid for significantly higher or lower Reynolds numbers than used in this study. Also, many parameters are not taken into account in this study, such as crosswind, surface roughness, atmospheric humidity and temperature and more.

5.6 Further Work

One goal of this study was to validate the use of OpenFOAM to create pressure distributions around airfoils, which again could be used for calculating the noise production. If the mesh size at the trailing edge is improved, all results, especially noise results, will most likely become in better agreement with references than shown in this report. The methodology from this study is then easily applicable for other airfoils and other operating conditions, and provides a simple way to study their noise production. It is easy to change parameters such as chord length, wind velocity and angle of attack in the different files attached with the applied OpenFOAM software. Equation 2.1 can be used for taking rotation of a wind turbine into account when deciding a representative relative wind velocity for the airfoils.

If the results are not sufficiently improved by improving the trailing edge meshes, other simple improvements may be added. A finer mesh and a larger iteration time can easily be applied, and give significantly more accurate results without unreasonably large computational capacity, given the short calculation time of the present study. It can also be experimented with other solvers than SimpleFoam, either from OpenFOAM or from another software package, using different methods than RANS equations and/or different turbulence models and noise models than the Spalart-Allmaras and Amiet. Other models have different assumptions and limitations, and may be more appropriate for some cases, for example a less "flat" airfoil.

There are also good possibilities for expanding the present model into modelling noise production from full wind turbines. A methodology suggested by [1] is to apply a strip theory, dividing a wind turbine blade into strips of airfoils and summing up all their noise contributions. Iso-radius cuts of the wind turbine are made to obtain inputs for the noise models. The methodology for calculating the noise from each strip is merely the same as for the airfoils in this study. However, rotation effects must be taken into account. A sum of noise levels from the different sources can be calculated by Equation 2.11. In addition, the sound level decreases with about 6 dB for each doubling of the distance, but is also affected by atmospheric parameters and type of terrain. If taking all this into account, it is possible to accurately simulate the noise pressure level at a given distance from a wind turbine. Effects of different atmospheric conditions can then be studied both for existing wind parks and during planning of new wind parks. This can help designing solutions that reduce noise production from wind parks, and improve the living conditions for local residents.

6 Conclusion

This study aimed to validate the use of a simple BlockMesh generator and OpenFOAM's SimpleFoam solver to produce pressure distributions which can be used as inputs for noise calculations around airfoils. The methodology has produced lift coefficient curves showing good agreement with references. Drag coefficients were generally too high, and pressure coefficients where in good agreement except for closer to the trailing edge. This is mainly because of a coarse and inaccurate mesh at the trailing edge. Since noise results were calculated close to the trailing edge, this inaccuracy can also explain some of the deviations from references here. However, some simple improvements in the BlockMeshes would most likely improve the results significantly. With such improvements, the methodology described in this report can be used as a simple, but reliable alternative for simulating noise production of airfoils. There is also a short way into expanding the methodology into simulating aerodynamic noise production from full wind turbines.

References:

[1] H. Bériot et al. *Assessment of statistical and stochastic approaches for the prediction of WT nearfield noise*. Deliverable Deliverable D4.1. EU: IVKDF, SINTEF AS, Fraunhofer, AWST, SISW, Feb. 19, 2020. (Visited on 04/18/2022).

[2] GWEC. *Global Wind Report 2021*. Årsrapport. Mar. 24, 2021. URL: https://gwec.net/global-wind-report-2021/ (visited on 02/13/2022).

[3] Marte Mørk. *Counter Currents: A Case Study of Wind Power Resistance at Frøya, Norway*. Master's Thesis. Marienlyst: NMBU, June 2021. URL: https://nmbu.brage.unit.no/nmbu-xmlui/bitstream/handle/11250/2827261/Counter%20Currents%20-%20A%20Case%20Study%20of%20Wind%20Power%20Resistance%20at%20Fr%C3%B8ya%20Norway%20-%20Marte%20M%C3%B8rk%202021.pdf?sequence=1 (visited on 05/02/2022).

[4] Daniel Shepherd et al. "Evaluating the impact of wind turbine noise on health-related quality of life". In: *Noise and Health* 13.54 (Jan. 9, 2011). Company: Medknow Publications and Media Pvt. Ltd. Distributor: Medknow Publications and Media Pvt. Ltd. Institution: Medknow Publications and Media Pvt. Ltd. Label: Medknow Publications and Media Pvt. Ltd. Publisher: Medknow Publications, p. 333. ISSN: 1463-1741. DOI: 10.4103/1463-1741.85502. URL: https://www.noiseandhealth.org/article.asp?issn=1463-1741;year=2011;volume=13;issue=54;spage=333;epage=339;aulast=Shepherd;type=0 (visited on 05/02/2022).

[5] S. Oerlemans, P. Sijtsma, and B. Méndez López. "Location and quantification of noise sources on a wind turbine". In: *Journal of Sound and Vibration* 299 (Feb. 6, 2007), pp. 869–883. DOI: 10.1016/j.jsv.2006.07.032. URL: https://reader.elsevier.com/reader/sd/pii/S0022460X06006316?token=81EF12F76B7C6FAC63C7510E03349DB6B5E0C44F7F926F852A2048CFCAB5AF5DCF0F0E3D3AB8368C494DC57EDA2F7A7D&originRegion=eu-west-1&originCreation=20220203092741 (visited on 02/03/2022).

[6] Yuan Tian. *Modeling of wind turbine noise sources and propagation in the atmosphere*. PhD Thesis NNT : 2016SACLY003. Paris: L'Universite Paris-Saclay, Aug. 25, 2016. URL: https://tel.archives-ouvertes.fr/tel-01335869v2 (visited on 02/03/2022).

[7] Yakut Cansev Küçükosman. *Semi-analytical approaches for the prediction of the noise produced by ducted wind turbines*. Final published version. Delft: Delft University of Technology, 2019. (Visited on 05/18/2022).

[8] Hasan Kamilya Jawahar, Yujing Lin, and Mark Savill. "Large eddy simulation of airfoil self-noise using OpenFOAM". In: *Aircraft Engineering and Aerospace Technology* (Nov. 2017). DOI: 10.1108/AEAT-05-2015-0130. (Visited on 03/06/2022).

[9] Yunus A. Cengel and John M. Cimbala. *Fluid Mechanics Fundamentals and Applications*. 3. New York, 2014. ISBN: 978-0-07-338032-2. (Visited on 02/15/2022).

[10] J. F. Manwell, J. G. McGowan, and A. L. Rogers. *Wind Energy Explained - Theory, Design and Application*. 2nd ed. Great Britain: John Wiley & Sons Ltd., 2009. ISBN: 978-0-470-01500-1.

[11] Imants Reba. "APPLICATIONS OF THE COANDA EFFECT". In: *Scientific American* 214.6 (1966). Publisher: Scientific American, a division of Nature America, Inc., pp. 84–93. ISSN: 0036-8733. URL: https://www.jstor.org/stable/24930967 (visited on 05/03/2022).

[12] World Hovercraft Organization. *DiscoverHover Curriculum Guide #8 - Bernoulli's Principle and the Coanda effect*. DiscoverHover CURRICULUM GUIDE #8 BERNOULLI'S PRINCIPLE AND THE COANDA EFFECT. 2004. URL: https://www.discoverhover.org/infoinstructors/guide8.htm (visited on 05/03/2022).

[13] Michel Make. "Predicting scale effects on floating offshore wind turbines". PhD thesis. Apr. 28, 2014.

[14] Bastian Rapp. *Microfluidics: Modeling, Mechanics and Mathematics - 1st Edition*. 1st. Dec. 1, 2016. ISBN: 978-1-4557-3141-1. URL: https://www.elsevier.com/books/T/A/9781455731411 (visited on 05/04/2022).

[15] using all aspects of the marketing mix He particularly enjoys writing content about product applications using all aspects of the marketing mix et al. *What are 1:1 and 1:3 Octave Bands? — Cirrus Research plc*. NoiseNews. Nov. 4, 2011. URL: https://www.cirrusresearch.co.uk/blog/2011/11/what-are-octave-and-third-octave-band-filters-on-a-sound-level-meter/ (visited on 05/04/2022).

[16] Statens forurensningstilsyn. *Støy fra vindmøller*. TA-nummer 1738/2000. 2021. URL: https://www.miljodirektoratet.no/globalassets/publikasjoner/klif2/publikasjoner/luft/1738/ta1738.pdf (visited on 02/26/2022).

[17] Tony F. W. Embleton. "Tutorial on sound propagation outdoors". In: *The Journal of the Acoustical Society of America* 100.1 (July 1996). Publisher: Acoustical Society of America, pp. 31–48. ISSN: 0001-4966. DOI: 10.1121/1.415879. URL: https://asa.scitation.org/doi/abs/10.1121/1.415879 (visited on 02/26/2022).

[18] *Retningslinje for behandling av støy i arealplanlegging*. In collab. with Klima-og miljødepartementet. Publisher: regjeringen.no. June 11, 2021. URL: https://www.regjeringen.no/no/dokumenter/retningslinje-for-behandling-av-stoy-i-arealplanlegging/id2857574/ (visited on 02/25/2022).

[19] J.D. Anderson. *Basic Philosophy of CFD*. Ed. by John F. Wendt. Berlin, Heidelberg: Springer, 2009. ISBN: 978-3-540-85056-4. DOI: 10.1007/978-3-540-85056-4_1. URL: https://doi.org/10.1007/978-3-540-85056-4_1 (visited on 02/10/2022).

[20] OpenFOAM. *OpenFOAM*. 2022. URL: https://www.openfoam.com/ (visited on 02/03/2022).

[21] Gabriela Carita. *Modelamiento de Ruido basado en la Presión con OpenFoam - Tutorial*. gidahatari. Nov. 16, 2018. URL: https://gidahatari.com/ih-es/modelamiento-de-ruido-basado-en-la-presin-con-openfoam-tutorial (visited on 02/11/2022).

[22] Idealsimulations. *Turbulence models in CFD - RANS, DES, LES and DNS*. Turbulence Models in CFD. Aug. 30, 2019. URL: https://www.idealsimulations.com/resources/turbulence-models-in-cfd/ (visited on 05/10/2022).

[23] Teymour Javaherchi. *Review of Spalart-Allmaras Turbulence Model and its Modifications*. Review. Mar. 12, 2010, p. 14. URL: https://tarjomefa.com/wp-content/uploads/2016/10/5491-English.pdf (visited on 04/12/2022).

[24] Yannick Rozenberg, Gilles Robert, and Stéphane Moreau. "Wall-Pressure Spectral Model Including the Adverse Pressure Gradient Effects". In: *AIAA Journal* 50 (Oct. 1, 2012), pp. 2168–2179. DOI: 10.2514/1.J051500.

[25] Yuan Tian, Benjamin Cotté, and Antoine Chaigne. "Wind Turbine Noise Modelling Based on Amiet's Theory". In: (Apr. 8, 2014), p. 13. URL: https://hal-ensta-paris.archives-ouvertes.fr//hal-00975237/document (visited on 05/11/2022).

[26] Seongkyu Lee and Augusto Villaescusa. "Comparison and Assessment of Recent Empirical Models for Turbulent Boundary Layer Wall Pressure Spectrum". In: *23rd AIAA/CEAS Aeroacoustics Conference*. _eprint: https://arc.aiaa.org/doi/pdf/10.2514/6.2017-3688. American Institute of Aeronautics and Astronautics, June 9, 2017. DOI: 10.2514/6.2017-3688. URL: https://arc.aiaa.org/doi/abs/10.2514/6.2017-3688 (visited on 05/19/2022).

[27] Kenneth Moreland. *The ParaView Tutorial*. 2018. URL: https://www.paraview.org/Wiki/images/b/bc/ParaViewTutorial56.pdf (visited on 02/03/2022).

[28] Thien Phan. *blockMesh an Airfoil*. blockMesh an Airfoil. 2022. URL: https://www.phanquocthien.org/mesh-geometry/blockmesh/airfoil (visited on 04/13/2022).

[29] OpenFOAM. *OpenFOAM: User Guide: Turbulent flow over NACA0012 airfoil (2D)*. URL: https://www.openfoam.com/documentation/guides/latest/doc/verification-validation-naca0012-airfoil-2d.html (visited on 02/25/2022).

[30] Ankit Rohatgi. *WebPlotDigitizer - Extract data from plots, images, and maps*. WebPlotDigitizer. Aug. 15, 2021. URL: https://automeris.io/WebPlotDigitizer/ (visited on 05/18/2022).

[31] Karim Oukassou et al. "Comparison of the power, lift and drag coefficients of wind turbine blade from aerodynamics characteristics of Naca0012 and Naca2412". In: *Procedia Manufacturing*. 12th International Conference Interdisciplinarity in Engineering, INTER-ENG 2018, 4–5 October 2018, Tirgu Mures, Romania 32 (Jan. 1, 2019), pp. 983–990. ISSN: 2351-9789. DOI: 10.1016/j.promfg.2019.02.312. URL: https://www.sciencedirect.com/science/article/pii/S2351978919303506 (visited on 05/12/2022).

[32] Charles L. Ladson. *Effects of Independent Variation of Mach and Reynolds Numbers on the Low-speed Aerodynamic Characteristics of the NACA 0012 Airfoil Section*. Google-Books-ID: PoU4AQAAIAAJ. National Aeronautics, Space Administration, Scientific, and Technical Information Division, 1988. 104 pp.

[33] Dimitris Gkiolas and Dimitrios Mathioulakis. "Aerodynamic Study of a NACA 64418 Rectangular Wing under Forced Pitching Motions". In: *Fluids* 6.11 (Nov. 2021). Number: 11 Publisher: Multidisciplinary Digital Publishing Institute, p. 394. ISSN: 2311-5521. DOI: 10.3390/fluids6110394. URL: https://www.mdpi.com/2311-5521/6/11/394 (visited on 04/27/2022).

[34] Jin Chen and Quan Wang. *Wind Turbine Airfoils and Blades: Optimization Design Theory*. Google-Books-ID: wWVCDwAAQBAJ. Walter de Gruyter GmbH & Co KG, Dec. 4, 2017. 392 pp. ISBN: 978-3-11-034438-7.

[35] W. Timmer and R.P.J.O.M. Rooij. "Some aspects of high angle-of-attack flow on airfoils for wind turbine application". In: (June 3, 2014). URL: https://www.researchgate.net/profile/W-Timmer/publication/228650605_Some_aspects_of_high_angle-of-attack_flow_on_airfoils_for_wind_turbine_application/links/00b49517645254ae07000000/Some-aspects-of-high-angle-of-attack-flow-on-airfoils-for-wind-turbine-application.pdf (visited on 05/06/2022).

[36] Thomas Buhl. *Research in aeroelasticity EFP-2007-II*. Risø-R-Report II. OCLC: 761004033. Roskilde: Risø DTU, 2009. URL: https://backend.orbit.dtu.dk/ws/portalfiles/portal/3549227/ris-r-1698.pdf (visited on 05/12/2022).

[37] H. Schlichting. *Boundary Layer Theory*. 1st ed. McGraw-Hill, 1979. ISBN: 0-07-055334-3. (Visited on 02/19/2020).